Editors' Suggestion Invited

First beam demonstration of a conduction-cooled Nb_3Sn superconducting rf photoinjector

Chunguang Jing,[1,*] Roman Kostin,[1] Yubin Zhao,[1] Pavel Avrakhov,[1] Ernie Knight,[1] Sam Posen,[2] Grigory Eremeev,[2] Timergali Khabiboulline,[2] Damon Bice,[2] Alexander Netepenko,[2] Gongxiaohui Chen,[3] Wanming Liu,[3] Eric Wisniewski,[3] Scott Doran,[3] John Power,[3] Tom Reid,[3] and Michael Kelly[3]

[1]*Euclid Beamlabs LLC, Bolingbrook, Illinois 60440, USA*
[2]*Fermi National Accelerator Laboratory, Batavia, Illinois 60510, USA*
[3]*Argonne National Laboratory, Lemont, Illinois 60439, USA*

(Received 31 July 2026; accepted 16 October 2026; published 12 November 2026)

We report on the first beam produced by the world's first conduction-cooled superconducting radio frequency (srf) photogun. Over the past 5 years, Euclid, working in collaboration with Fermilab and Argonne National Laboratory, has been developing a continuous-wave (cw), 1.5-cell, MeV-scale, conduction-cooled srf photogun operating at 1.3 GHz. The primary objective of this effort is to demonstrate ultrastable electron beams for ultrafast electron microscopy/diffraction (UEM/UED) applications, enabled by the exceptional shot-to-shot stability achievable with srf technology compared to room-temperature rf photoguns. Although srf systems were historically too costly for industrial deployment, two recent advancements: Nb_3Sn coatings and conduction cooling, have dramatically reduced system complexity and operating costs. This srf photogun is designed to deliver true cw rf operation while dissipating only ~2 W of rf power, eliminating the need for a high-power rf system and significantly reducing facility footprint. This srf photogun also features a raised Nb_3Sn backwall serving as the photocathode, removing the need for an external cathode insert. cw rf operation with limited repetitive beam has been demonstrated. In this paper, we present the first beam results from this system along with its cooldown performance, Q-slope behavior, synchronization characteristics, and initial beam parameters.

DOI: 10.1103/bgwr-36wy

I. INTRODUCTION

Ultrafast electron diffraction (UED) and ultrafast electron microscopy (UEM) have become powerful tools for investigating structural dynamics in materials, chemical systems, and biological specimens with femtosecond temporal resolution [1–4]. Most existing UED and UEM instruments are based on transmission electron microscope technology and operate at electron energies ranging from tens to hundreds of kiloelectronvolts. These systems have enabled important advances in the direct observation of ultrafast structural transformations; however, their performance is fundamentally constrained by strong space-charge effects at low beam energies, which limit the achievable bunch charge, temporal resolution, and beam brightness [5,6].

To overcome these limitations, significant effort has been devoted to the development of relativistic or MeV-scale UED and UEM systems [7–9]. The increased beam rigidity at relativistic energies substantially suppresses space-charge-induced emittance growth and bunch lengthening, enabling higher bunch charge, improved temporal resolution, and enhanced penetration through thicker samples. Several MeV-UED facilities based on normal-conducting radio-frequency (rf) photoinjectors have successfully demonstrated sub-100 fs temporal resolution and opened new opportunities to study weak-scattering processes, irreversible phenomena, and complex material dynamics [3]. Despite these advantages, the beam throughput of existing MeV-UED systems remains limited because most normal-conducting rf photoinjectors operate at repetition rates ranging from a few Hz to several kHz. Consequently, experiments often require long acquisition times, particularly when investigating weak diffraction signals, low scattering cross sections, or dose-sensitive specimens.

*Contact author: c.jing@euclidtechlabs.com

Published by the American Physical Society under the terms of the Creative Commons Attribution 4.0 International license. Further distribution of this work must maintain attribution to the author(s) and the published article's title, journal citation, and DOI.

Superconducting rf (srf) photoinjectors offer a promising path toward overcoming this limitation [10–13]. Owing to their extremely low rf surface resistance, srf cavities can operate in continuous-wave (cw) mode while dissipating only a few watts of rf power. In principle, the achievable bunch repetition rate is limited primarily by the drive laser system, enabling orders-of-magnitude higher average beam flux than conventional normal-conducting rf photoguns. In addition, srf cavities provide exceptional amplitude and phase stability, making them attractive candidates for next-generation UED and UEM facilities that require both high beam quality and high data throughput.

Over the past two decades, several srf photoinjectors have been developed for accelerator and light-source applications. Notable examples include the BNL srf gun developed for the coherent electron cooling program [10], the ELBE srf gun at HZDR [11], and subsequent photoinjector developments at NPS, HZB, and other laboratories [12–15]. These systems successfully demonstrated the capability of srf technology to generate high-brightness electron beams with excellent stability and cw operation. However, all existing srf photoinjectors rely on liquid-helium cryogenic infrastructure, requiring large cryogenic plants, significant operational expertise, and substantial facility resources.

Recent advances in Nb_3Sn-coated srf cavities and conduction-cooling technology have created an opportunity to dramatically simplify srf accelerator systems [16–18]. Nb_3Sn cavities can maintain high quality factors at temperatures accessible to commercial cryocoolers, while conduction cooling eliminates the need for liquid helium by extracting rf losses through high-conductivity thermal links [18,19]. In recent years, conduction-cooled srf cavity demonstrations at Fermilab, Cornell, and Jefferson Lab have established the technical foundation for compact, cryogen-free srf accelerators [18,20,21]. These developments open the possibility of deploying srf photoinjectors outside large accelerator facilities and integrating them into laboratory-scale scientific instruments.

Motivated by these advances, Euclid Beamlabs, in collaboration with Fermilab and Argonne National Laboratory, has developed a 1.3 GHz, 1.5-cell conduction-cooled srf photoinjector intended for MeV-UED and UEM applications. The photoinjector incorporates a Nb_3Sn-coated cavity cooled entirely by a commercial cryocooler and employs a raised Nb_3Sn back wall as the photocathode, eliminating the need for a removable cathode insert. Earlier work demonstrated successful conduction-cooled operation of the cavity and cryomodule and established the thermal, magnetic, and rf performance required for beam generation [22,23].

In this paper, we report the first beam generation of the developed conduction-cooled srf photoinjector. We describe the photogun and cryomodule design, summarize the thermal and rf performance achieved during cryogenic operation, discuss the engineering challenges encountered during beamline integration, and present the first photoemission beam generated from the Nb_3Sn photocathode. Earlier publications from this collaboration reported individual milestones in the cavity design, Nb_3Sn coating, vertical testing, and conduction-cooling development. In the present paper, these earlier results are summarized only as necessary background. The principal new contributions are the final cryomodule and beamline integration, the engineering improvements implemented during commissioning, and, most importantly, the first generation and transport of a photoemitted electron beam from the conduction-cooled Nb_3Sn srf photogun. These results establish the feasibility of cryogen-free srf photoinjectors and represent an important milestone toward practical high-repetition-rate MeV-UED and UEM facilities.

II. PHOTOGUN AND CRYOMODULE DESIGN

A. 1.5-cell 1300 MHz photogun

The accelerating structure is a 1.3-GHz superconducting photogun consisting of a photocathode half-cell followed by a TESLA-type full cell. The cavity was developed for high-repetition-rate UED and UEM applications, where both beam energy and energy spread are critical performance parameters. Unlike many photoinjector applications that prioritize maximum accelerating gradient, UED and UEM sources require the simultaneous achievement of high beam energy and extremely low energy spread to preserve temporal and spatial resolution.

The cavity design process began with an investigation of conventional 1.X-cell geometries having different photocathode half-cell lengths. For each geometry, particle-tracking simulations were performed to determine the beam energy as a function of laser injection phase for different accelerating gradients. To evaluate the energy-spread performance, the derivative of beam energy with respect to the injection phase, $dE_b/d\varphi$, was also examined. Since the final energy spread is closely related to the local rf curvature experienced during photoemission, the minimum energy spread is expected to occur near the operating point where $dE_b/d\varphi$ approaches zero.

The analysis revealed that the phase corresponding to maximum beam energy generally differs from the phase yielding minimum energy spread. For a conventional half-cell geometry, no single operating point simultaneously provided both maximum beam energy and minimum energy spread [24]. Although shortening the half-cell length moved the two optimum phases closer together, it also reduced the achievable beam energy. Similar findings were previously reported in Ref. [25].

To overcome this limitation, a modified cathode geometry was introduced. A raised plateau was incorporated

into the cathode region of the back wall, producing a localized modification of the accelerating field near the emission surface while preserving the overall rf efficiency and resonant frequency of the cavity. The resulting field profile allows the phase corresponding to maximum beam energy to more closely coincide with the phase yielding minimum energy spread. In addition, the inward-sloped back-wall geometry provides enhanced mechanical stiffness compared with a conventional flat cathode configuration.

The final cavity design corresponds to a shorter half cell geometry incorporating the raised-cathode structure. Electromagnetic simulations predict 20 MV/m of accelerating field on axis [see Fig. 1(b)], corresponding to a peak surface electric field of 23.5 MV/m and a peak surface magnetic field of 43.3 mT. Other parameters are summarized in Table I. Here, E_{acc} denotes the cavity accelerating gradient, E_{cathode} the electric field at the cathode surface, and E_{s} the surface electric field. For this cavity geometry, $E_{\mathrm{cathode}} \approx 2E_{\mathrm{acc}}$. Under nominal operating conditions, beam-dynamics simulations predict a beam energy of approximately 1.6 MeV with an energy spread in the low 10^{-5} range, meeting the requirements for high-resolution UED and UEM applications [24,26].

The final cavity and its electric-field profile are shown in Fig. 1. rf power is coupled into the cavity through a fixed coaxial fundamental power coupler (FPC), while an independent pickup probe provides the cavity field signal for the low-level rf (LLRF) control system. Because the photogun is intended for UED and UEM applications with negligible beam loading, the coupler was designed for near-critical coupling at the operating temperature. The FPC employs a Type-N coaxial connector to accommodate the forward rf power, whereas the pickup utilizes an SMA probe optimized to achieve an external quality factor of approximately 1.7×10^{11}. Electromagnetic simulations were performed using CST and COMSOL to optimize the coupling coefficients and antenna geometries. Particular attention was given to minimizing crosstalk between the FPC and pickup probe, since both ports are located near the beam exit. The final design achieved an rf isolation of approximately −132 dB while maintaining the desired pickup coupling, ensuring that the LLRF system accurately measures the cavity field with minimal contamination from the input rf signal.

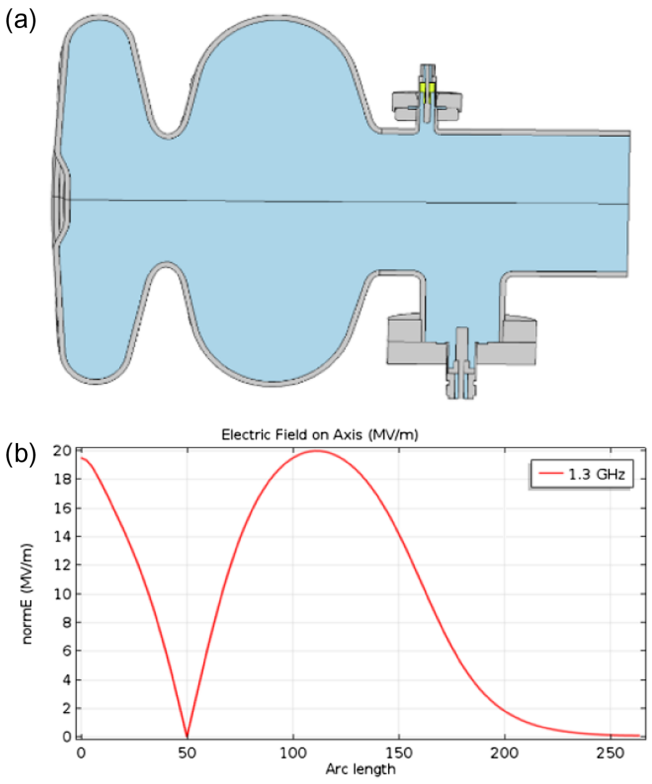


FIG. 1. Complete cavity design with the main rf coupler and signal pickup (a) and the accelerating field on axis (b).

TABLE I. Design and simulated major rf and beam parameters of the photogun.

Parameter	Design value
Frequency	1300 MHz
Effective length	160 mm
Q_0 at 4 K ($R_{\mathrm{res}} = 10$ nΩ)	1.61×10^{10}
R/Q	176.9 Ω
Geometry factor	232 Ω
Wall power dissipation, P_w	0.9 W
Peak E_{cathode}	20 MV/m
Peak E_s	23.5 MV/m
Peak B_s	43.3 mT
E_{acc}	10 MV/m
Beam energy	1.6 MeV
Charge per bunch	5 fC
Relative energy spread (100 fs rms laser pulse)	2×10^{-5}
Normalized beam emittance (36 μm rms laser spot)	6 nm

The cavity back wall serves directly as the photocathode. This approach eliminates the complexity associated with removable cathode inserts and avoids potential issues related to rf contact reliability, multipacting, and vacuum contamination. The entire cavity, including the cathode region, was subsequently coated with Nb_3Sn to enable cryocooler-based operation near 4 K. To evaluate the feasibility of using Nb_3Sn directly as the photocathode, quantum-efficiency (QE) measurements were performed on witness coupons. At room temperature and a vacuum level of approximately 1×10^{-7} Torr, a QE of approximately 1×10^{-7} was measured at a wavelength of 255 nm, corresponding to roughly one order of magnitude lower QE than that measured for pure Nb under the same conditions. The measured work function of the Nb_3Sn surface was approximately 3.8 eV. Despite the relatively

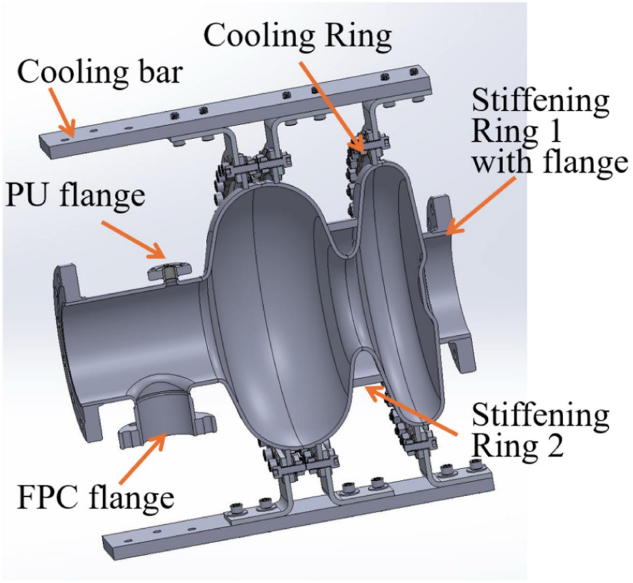


FIG. 2. Engineering design of the photogun cavity with stiffening rings and cooling bars.

low QE, the required bunch charge for UED/UEM applications is sufficiently small that the photocathode can be driven using commercially available UV laser systems, while retaining the advantages of a robust, fully superconducting cathode configuration.

Mechanical analyses were performed to ensure compatibility with vacuum loading, cryogenic operation, and microphonic requirements. Two niobium stiffening rings were incorporated into the cavity structure to reduce mechanical stress and Lorentz-force detuning. Additional longitudinal reinforcement was added to improve rigidity and suppress vibration modes. Finite-element simulations predicted a maximum mechanical stress below 30 MPa and a lowest structural resonance near 311 Hz, consistent with conventional srf cavity practice.

Figure 2 shows the final engineering design of the cavity. To facilitate conduction cooling, niobium cooling rings were welded around the cavity equators. These rings provide thermal interfaces between the cavity and external high-conductivity thermal links connected to the cryocooler cold head.

B. Conduction-cooled cryomodule

A compact cryogen-free cryomodule was developed specifically to support conduction-cooled operation of the 1.3 GHz srf photogun. Unlike conventional srf photoinjectors that rely on liquid-helium cryogenic systems, the present design employs a commercial two-stage cryocooler as the sole refrigeration source. The cryomodule was designed to provide sufficient cooling capacity for both the static thermal load and the rf power dissipated in the Nb_3Sn-coated cavity while maintaining a compact footprint suitable for laboratory-scale UED and UEM facilities.

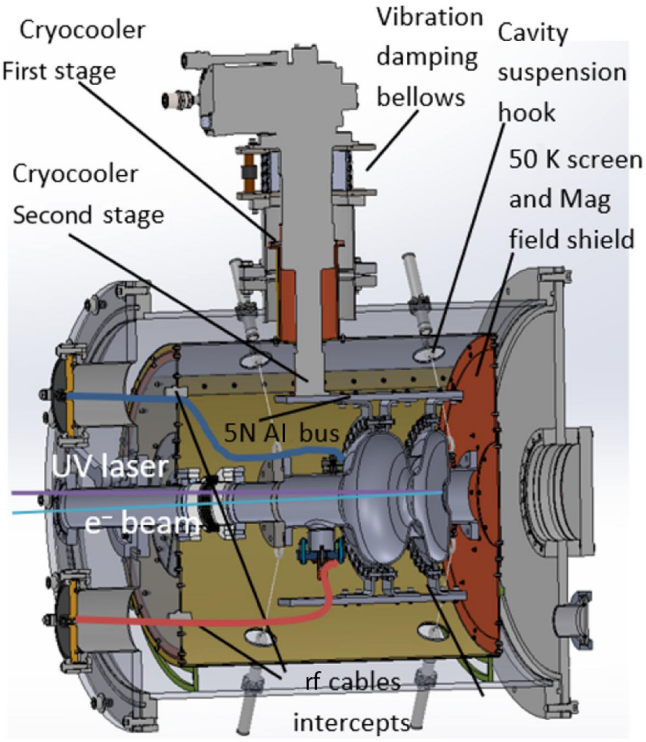


FIG. 3. Engineering design of the conduction-cooled srf photogun cryomodule.

The cryomodule consists of a cylindrical vacuum vessel, thermal radiation shield, magnetic shielding system, cavity suspension structure, and cryocooler assembly. A cylindrical geometry was selected to maximize structural rigidity while minimizing material usage and fabrication complexity. The vacuum vessel has an outer diameter of 24 inch, providing adequate space for the cavity, thermal links, magnetic shield, and associated rf and diagnostic components. A three-dimensional rendering of the cryomodule is shown in Fig. 3. The cavity is suspended inside the vacuum vessel using low-thermal-conductivity supports and is thermally connected to the cryocooler through dedicated conduction-cooling links.

The cavity cooling scheme is based on high-purity aluminum thermal links connecting the second stage of the cryocooler to niobium cooling rings welded around the cavity equators. The thermal links were fabricated from 5 N aluminum, whose thermal conductivity exceeds 3–5 kW/m/K at cryogenic temperatures. This approach provides a low thermal resistance path between the cavity and the cryocooler. The cooling rings were incorporated into the cavity design from the outset and serve as the primary thermal interfaces for removal of rf losses from the superconducting structure.

Comprehensive thermal analyses were performed using temperature-dependent material properties and realistic thermal contact resistances. For the design operating point of $E_{acc} = 10$ MV/m and $Q_0 \sim 1.6 \times 10^{10}$, the cavity

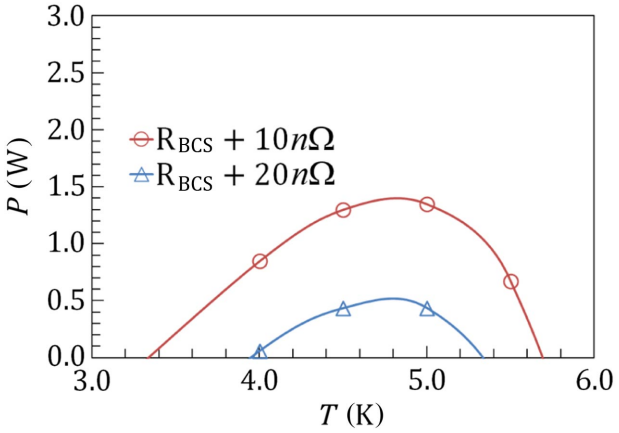


FIG. 4. The excess power calculated from the cooling capacity curve of a 2 W, SRDK-418 cryocooler and rf power dissipation in the srf photogun operating at 10 MV/m of accelerating gradient under different residual resistances.

rf dissipation was predicted to remain below 1 W, allowing stable operation near 4 K using a single commercial cryocooler. Figure 4 shows simulation results of the excess power available from a single cryocooler. The calculation indicates that, in the case of 20 nΩ additional surface resistance, R_{res}, on top of R_{BCS}, which corresponds to the expected $Q_0 \sim 9 \times 10^9$, the cavity stabilizes near 4.8 K at the operating point with approximately 0.5 W of additional cryocooler capacity. Thermal calculations showed that the available cryocooler capacity exceeds the combined static and dynamic heat loads under nominal operating conditions. A Sumitomo SRDK-418 Gifford-McMahon cryocooler was selected for the cryomodule. The cryocooler provides approximately 2 W of cooling capacity at 4.2 K on the second stage and sufficient refrigeration power at the first stage to support the thermal radiation shield. The cryocooler is mounted through an 8-inch-diameter ConFlat port and connected to the cryomodule through a bellows assembly that accommodates thermal contraction and reduces vibration transmission to the cavity.

To minimize radiative heat transfer to the superconducting cavity, a copper thermal shield operating near 30 K surrounds the cold mass and is thermally anchored to the first stage of the cryocooler. Multilayer insulation and thermal intercepts are incorporated throughout the cryomodule to reduce conductive heat leakage through the beamline, support structures, and rf cables. The estimated static heat load to the 4-K stage was below 0.2 W, while the total load intercepted at the 30-K shield was approximately 20 W. These values are summarized in Table II.

Because trapped magnetic flux can significantly degrade the rf performance of Nb_3Sn cavities, particular attention was given to magnetic shielding. The cryomodule incorporates a cylindrical cryogenic magnetic shield located outside the thermal shield and surrounding the cavity region. Simulations predicted that the shielding system would reduce the ambient geomagnetic field by approximately 2 orders of magnitude. During commissioning, magnetic-field measurements performed using a fluxgate magnetometer demonstrated that the residual field in the cavity region was below 10 mG at room temperature after installation of magnetic shunts, meeting the design requirement for high-Q_0 operation. A solid, large-area contact where the magnetic-shield cylinder surrounding the cold-head insert meets the magnetic-shielding enclosure outside the thermal shield played a critical role in achieving this goal [26].

TABLE II. Simulated cryomodule static heat loads.

Source	30-K zone (W)	4-K zone (W)
Radiation	2	0.01
Beam pipe	17	0.03
Suspension	N/A	0.05
rf cables	0.8	0.05
Total	20	0.14

The cryomodule was commissioned prior to cavity installation. Cooldown tests demonstrated successful operation of the cryogenic system, with the unloaded second stage reaching a temperature of approximately 2.5 K and the thermal shield stabilizing near 28 K. These results were consistent with the thermal design calculations and confirmed the readiness of the cryomodule for integration with the Nb_3Sn srf photogun.

III. CAVITY PERFORMANCE

The development of the conduction-cooled srf photogun involved multiple stages of cavity fabrication, surface processing, Nb_3Sn coating, vertical testing, and cryomodule integration. A comprehensive description of the cavity fabrication procedure, vertical test configuration, and rf performance measurements has been reported previously in Refs. [22,27]. In this section, only the results most relevant to the first-beam demonstration are summarized.

The 1.3 GHz photogun cavity was fabricated from RRR-300 niobium and initially evaluated prior to Nb_3Sn coating. Following bulk chemical polishing, high-pressure rinsing, and heat treatment, the cavity underwent two vertical tests at Fermilab. During the second test, a peak E_{acc} of 22 MV/m was achieved, corresponding to approximately 44 MV/m on the cathode surface, with a maximum quality factor of 1.2×10^{10} at 2 K. These results verified both the rf design and the effectiveness of the surface preparation procedures.

Following qualification of the bare niobium cavity, the photogun was coated with Nb_3Sn at Fermilab to enable operation using cryocooler-based conduction cooling. Subsequent vertical testing revealed a significant reduction in rf performance compared with the bare niobium cavity.

Detailed investigations indicated that the cavity experienced mechanical deformation (causing cracks in the Nb_3Sn coating) during the fixture installation process, resulting in frequency shifts and degraded rf characteristics. Following removal of the degraded first Nb_3Sn coating, the cavity was recoated. Frequency monitoring during fixture assembly confirmed that the mechanical deformation observed during the first coating had been eliminated, with the cavity frequency measured at 1298.09 MHz at room temperature after coating. Vertical testing of the recoated cavity showed improved rf performance, achieving an accelerating gradient of 6 MV/m. No field emission over the tested electric field range or multipacting-induced power oscillation was observed. Subsequent analysis identified silicon contamination of the Nb_3Sn layer during the deposition, which was considered a likely contributor to the reduced Q_0.

Despite the reduced gradient, the measured quality factor remained sufficient to support conduction-cooled operation. The cavity was therefore integrated into the cryomodule and used for system-level commissioning and beam generation experiments. The principal objective of the subsequent effort was to demonstrate stable cryogenic operation, verify thermal and magnetic performance of the cryomodule, and establish photoemission from the integrated Nb_3Sn photocathode. Following assembly, the cavity was installed into the conduction-cooled cryomodule and cooled using a commercial two-stage cryocooler. During initial commissioning, the cryogenic system reached temperatures consistent with the thermal design model, while magnetic-field measurements confirmed residual fields below 10 mG in the cavity region. Figure 5 shows the measured cooldown history. Additional optimization of thermal interfaces, support structures, magnetic shielding, and instrumentation was subsequently carried out during beamline integration. These improvements are discussed in the following section.

The cavity performance achieved after installation into the cryomodule is summarized in Fig. 6, which compares the rf behavior observed during vertical testing and one of the best controlled conduction-cooled tests. The low-field Q_0 values were approximately 6×10^9 in both

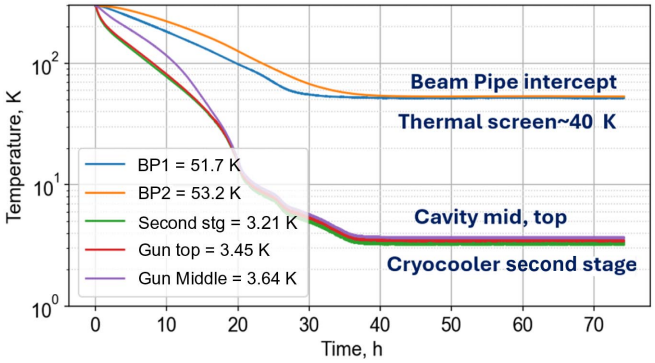


FIG. 5. Cooldown history at different locations.

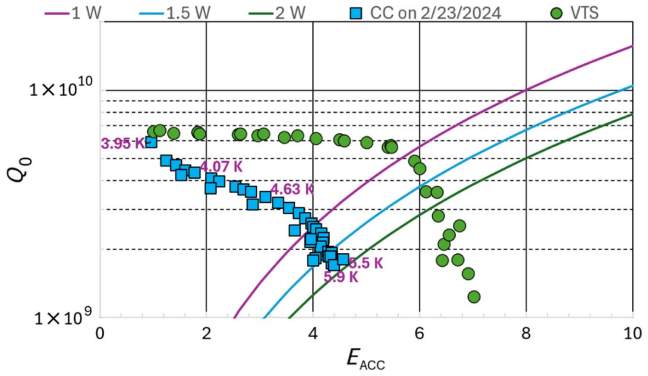


FIG. 6. Measured Q slopes of two rf tests of the Nb_3Sn srf photogun: Fermilab vertical test stand (VTS) and conduction-cooled (CC) test at Euclid on 2/23/2024. To increase readability without losing key information, the selected temperatures on the middle of the cavity are labeled in the CC test. Three cavity constant power dissipation curves are also shown.

the vertical test and the conduction-cooled test, demonstrating similar cavity conditions, such as temperature and external magnetic field, at a low rf feeding. The subsequent degradation in Q factor with the gradient is caused by the cavity temperature increasing with the higher electric gradient as the system does not have sufficient cooling capacity to compensate for the degraded Q factor. Another contributing factor is the FPC coupling which was tuned for $Q_{ext} \sim 10^{10}$, causing additional reflected power, which inevitably increased power dissipation in the FPC power cable, contributing to cavity temperature rise as well. The controlled cooldown process near the critical temperature was performed by cycling the cryocooler on and off while monitoring the temperature at two cavity locations to maximize cooldown uniformity. In practice, the cryocooler was cycled with approximately 5 s intervals between on/off commands. Between 20 and 14 K, a typical cooldown rate of approximately 0.5 K per 10 s was achieved. Because this manually controlled procedure was not fully reproducible, further improvement of the cooldown control is planned. Three different cavity power dissipation lines are also plotted in Fig. 6. rf testing supported operation up to 4.5 MV/m before exceeding the cooling capacity.

IV. BEAMLINE INTEGRATION AND SYSTEM IMPROVEMENT

The beam generation experiment for the conduction-cooled Nb_3Sn srf photogun was ultimately carried out at the Argonne Wakefield Accelerator (AWA) facility, selected for its proximity to the development site and availability of a 300-fs high-power UV laser. Beyond that, the AWA facility also offers a flexible accelerator R&D environment that enabled rapid integration, commissioning, and iterative optimization of this first-of-its-kind

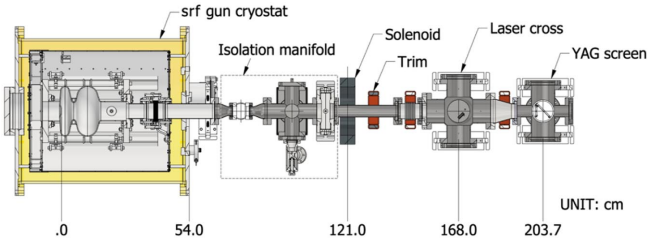


FIG. 7. Beamline layout of the conduction-cooled srf photogun at AWA.

photogun. A dedicated beamline was designed (refer to Fig. 7) and installed in the AWA bunker, with supporting infrastructure prepared in advance. Beam dynamics simulations indicated reduced beam energy compared to the design expectation due to Nb_3Sn coating degradation, limiting the achievable accelerating gradient to approximately 45% of the nominal value.

The srf photogun cryomodule and control systems were delivered to AWA in April 2024. Critical assembly steps, including integration of the valve system and beam pipe, were performed in a cleanroom environment to minimize particulate contamination prior to installation. Following installation, an initial standalone cooldown test of the cryostat without the cavity confirmed proper operation of the cryocooler and thermal system after transport.

During subsequent photogun integration, a mechanical imbalance was identified due to the additional mass of the valve and beam pipe assembly, which shifted the center of gravity beyond the load capacity of the original support structure. In the initial design, the cavity assembly was supported directly from the cryostat wall through the radiation shield without any thermal intercept. To minimize parasitic heat load to the cold mass, the support structure employed low-thermal-conductivity materials with a small cross-sectional area. While thermally effective, this approach provided insufficient mechanical stiffness for the increased load. The support structure was therefore completely redesigned and divided into two independent systems. The first supports the radiation shield from the cryostat wall, while the second supports the cold mass (cavity assembly) from the radiation shield. Both support systems are independently adjustable, greatly simplifying alignment during assembly. More importantly, the thermal gradient across the cold-mass support was reduced from approximately 300 to about 50 K, allowing the use of a substantially more robust mechanical design with reduced parasitic heat load. The cavity support employs adjustable tie rods and rotating joints, providing sufficient degrees of freedom to safely and precisely align the cavity assembly with the cryocooler cold finger during installation (refer to Fig. 8). Subsequent cooldown tests confirmed improved thermal performance while maintaining excellent mechanical stability. The additional radiation-shield support contributed only approximately 2 W to the first-stage heat load, resulting in a stable first-stage temperature of 27 K. This performance was verified during cryomodule testing without the cavity installed.

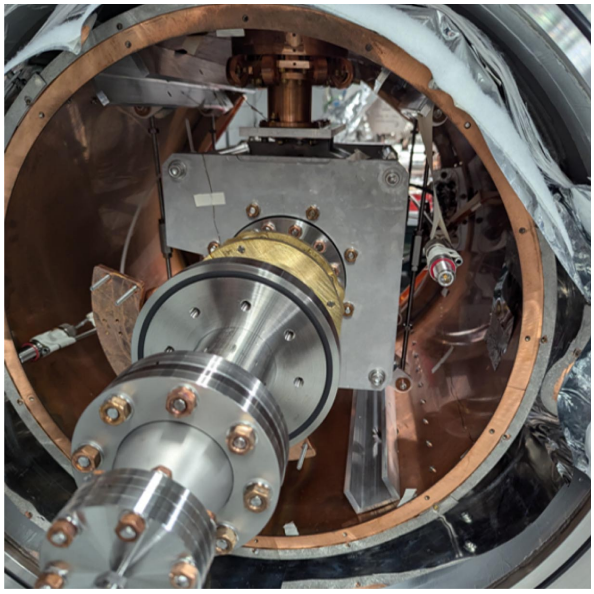


FIG. 8. Installation process with improvement measures to reduce residual magnetic fields and thermal leakage.

Following these modifications, the cavity assembly was installed into the cryomodule and successfully cooled down. The beam pipe assembly was thermally intercepted at the radiation shield, contributing approximately 20 W to the first-stage heat load. Including the support structure, the total first-stage heat load reached approximately 23 W, increasing the first-stage temperature to 31 K. This result is in excellent agreement with the thermal model presented in Table II, which predicted a 20 W heat load and a corresponding first-stage temperature of approximately 30 K. It is worth noting that the radiation shield itself operates approximately 10 K warmer because of the finite thermal conductivity of the thermal screen (see Fig. 5).

Initially, the cavity reached a minimum temperature of only 5.8 K. After reconditioning the aluminum and copper thermal-link contact surfaces by mechanical polishing, cleaning, and prompt reassembly, the operating temperature was reduced to 3.7 K, decreasing the temperature difference between the second-stage cold head and the cavity to only 0.4 K. The elevated temperature during the initial cooldown was primarily attributed to naturally formed aluminum oxide layers on the thermal-link contact surfaces after prolonged air exposure. These oxide layers were removed by mechanical polishing prior to reassembly, along with improved surface roughness and flatness, significantly improving the thermal contact conductance. Some instability in cavity performance was also observed during the initial tests, as the cavity was not actively pumped for an extended period of time. The issue was resolved after cavity pump down.

During the subsequent upgrade, all magnetic materials in the vicinity of the cavity were systematically eliminated. The original 316L stainless-steel support rods were found to exhibit residual magnetization of approximately 400 mG and were replaced with titanium rods. In addition, the rf cables were demagnetized, reducing their residual magnetic field from approximately 700 to 30 mG. These components were located not far from the cavity, but not in its immediate vicinity. The magnetic field on the cavity surface was around 5 mG in the area of high rf magnetic field at room temperature. Note that, in an earlier cooldown, performed before the final demagnetization, an abrupt change in the measured magnetic field was observed as the cavity crossed the superconducting transition, consistent with flux expulsion. The trapped magnetic flux may vary depending on the controlled cooldown process.

Final beamline assembly required controlled exposure of the cavity to atmosphere. As shown in Fig. 9, a localized clean environment was established in the AWA bunker using a custom class-10 clean hood, while critical subassemblies, such as the gate-valve system, were prepared in a class-10 cleanroom. The gate-valve assembly, incorporating a pumped intermediate chamber, enabled staged vacuum commissioning: the srf cavity was brought to ultrahigh vacuum while maintaining isolation from downstream beamline construction. This approach ensured cleanliness and vacuum integrity throughout integration.

Overall, beamline preparation established a stable and contamination-controlled platform for beam generation while addressing key engineering challenges in mechanical support, thermal management, vacuum performance, and magnetic shielding that are essential for conduction-cooled srf photogun operation.

Figure 10 shows the schematic of the LLRF-laser synchronization system. The LLRF system is based on an NI PXI platform, in which an FPGA-based IF transceiver, together with an IQ modulator and demodulator,

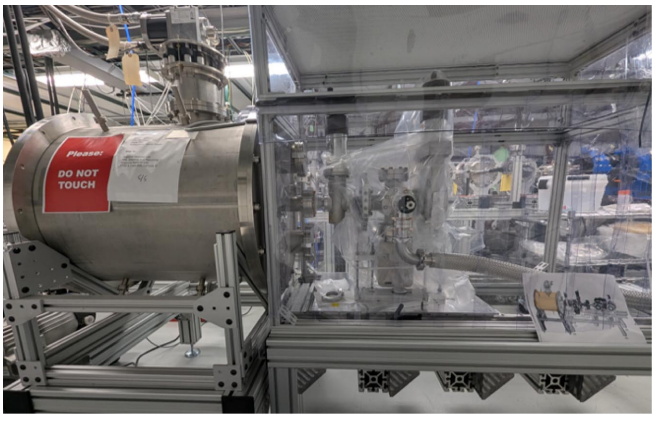


FIG. 9. Gate-valve assembly connected to the srf cryomodule in the customized clean hood.

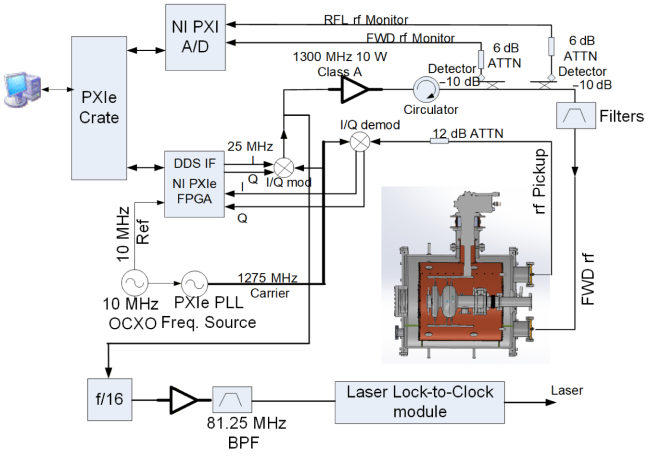


FIG. 10. Diagram of the LLRF system.

generates an rf signal that dynamically tracks the srf cavity resonance frequency according to the cavity pickup signal. The forward and reflected powers are monitored via A/D converters. The 1.3 GHz output of the IQ modulator is split into two paths. One path is amplified by a 1.3 GHz rf power amplifier to drive the srf cavity, while the other is sent to a divide-by-16 frequency divider, with appropriate amplification and filtering, to generate the 81.25 MHz signal required by the laser reference clock input. The bandwidth of the reference clock input is sufficient to accommodate that of the forward rf signal.

In the final controlled cooldowns, the system achieved stable cryogenic operation with a cold-head temperature of 3.3 K and cavity temperature below 3.7 K, with minimal thermal gradients. rf testing yielded a quality factor of approximately 4×10^9 at low field and supported operation at $E_{\mathrm{acc}} \geq 4.5$ MV/m with 10 W of the rated rf amplifier output. Beam-dynamics simulations predict a maximum beam energy of approximately 400 keV at $E_{\mathrm{acc}} \approx 4.5$ MV/m for an appropriate laser injection phase. The ultimate limitation in the conduction-cooled configuration was the available cooling capacity of the single cryocooler combined with the degraded Q_0. Beyond approximately $E_{\mathrm{acc}} = 4.5$ MV/m, additional rf power primarily increased the cavity temperature rather than the gradient, until the LLRF system could no longer maintain resonance lock. Figure 11 shows the results before and after the improvements implemented during beamline construction.

V. FIRST BEAM GENERATION

The first beam experiment was conducted in December 2025. A 262 nm UV laser was aligned to the center of the cathode region. The measured vacuum pressure at exit of the srf cavity was 4×10^{-9} Torr. During the beam test, the laser pulse energy was approximately 3.7 μJ, with a spot size of approximately 10 mm in diameter on the cathode. The beam test was operated at 2 Hz because of the AWA

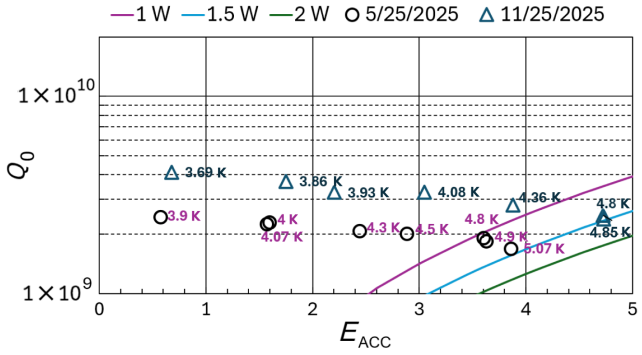


FIG. 11. Measured Q slopes summarizing two rf tests of the Nb_3Sn srf photogun before (5/25/2025) and after (11/25/2025) the full beam pipe assembly. Temperatures on the middle of the cavity are labeled at each measurement point. Three cavity constant power dissipation curves are also shown.

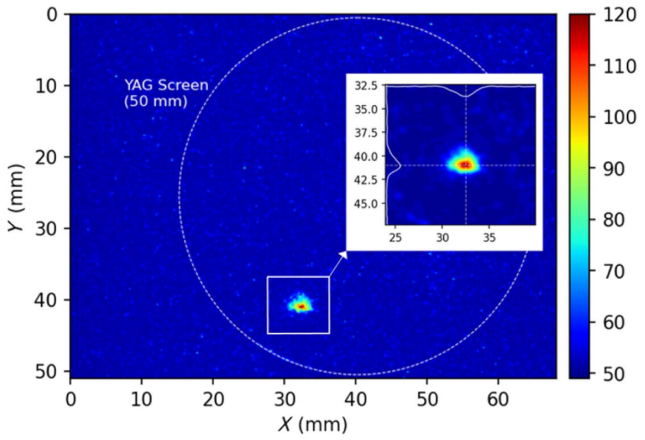


FIG. 12. First photoemission beam captured at the downstream YAG screen.

data-acquisition configuration. Assuming a QE of 1×10^{-7}, comparable to the room-temperature witness-sample measurement, the 3.7-μJ pulse would correspond to approximately 80 fC; however, no charge diagnostic with sufficient sensitivity for the expected fC-level bunch charge was available, and the charge and effective QE of the installed cathode were not quantitatively measured. For the 5-fC UED design charge, the corresponding laser pulse energy would scale to about 0.23 μJ, or about 0.23 W of incident UV power at 1 MHz. The photoemission origin of the beam was verified by repeatedly opening and closing the UV-laser shutter, i.e., the beam disappeared when the laser was blocked and reappeared when it was restored. The beam was observable for approximately 80% of the 4-h operating period; intermittent beam loss was primarily associated with unstable laser-rf synchronization.

A measured cw forward rf power of 7 W was delivered to the cavity. After accounting for the reflected power, the net power dissipated in the cavity was estimated to be approximately 1.4 W, resulting in a cavity temperature of 4.8 K. Note that the rf-cable loss was calibrated at low power and may differ from the loss under high-field operating conditions. After a brief tuning period, the first photoemitted beam was successfully observed on the downstream YAG screen, as shown in Fig. 12.

Phase scans were attempted; however, synchronization issues in the control system prevented stable locking between the drive laser and the rf signal. As a result, a clean phase-scan dataset could not be obtained. In addition, because the beam energy was significantly lower than the design value, no dedicated energy spectrometer was available in the relevant range. Instead, the beam energy was estimated using a trim magnet (Fig. 13) to deflect the beam. The axial magnetic-field profile of the trim magnet was measured, and the field strength was calibrated as a function of drive current. The distance from the center of the trim magnet to the downstream YAG screen was 0.695 m. The beam-deflection angle was determined from the measured centroid displacement on the YAG screen, and the beam momentum was calculated from the corresponding integrated magnetic field. This analysis yielded an estimated beam energy of approximately 190 keV, which corresponds to $E_{\mathrm{cathode}} \approx 7$ MV/m (i.e., $E_{\mathrm{acc}} \approx 3.5$ MV/m), as inferred from the beam simulations.

The dominant systematic uncertainty arises from the unknown beam trajectory through the trim magnet,

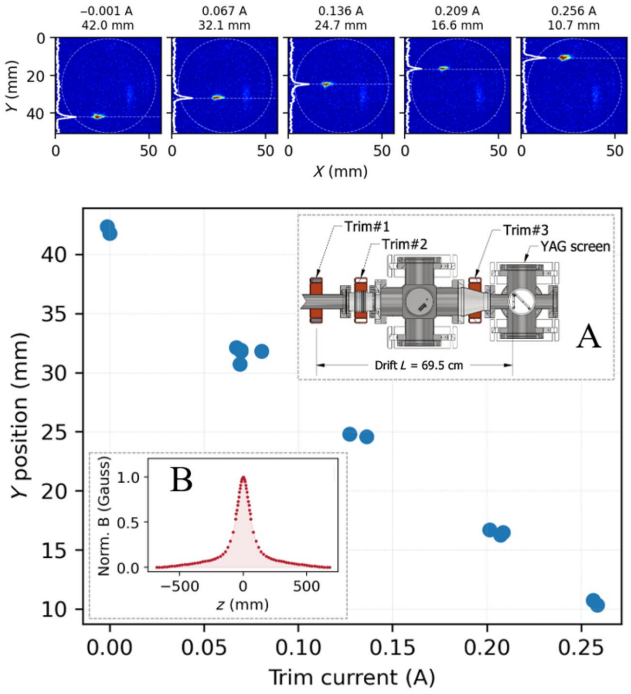


FIG. 13. Energy measurement using a trim magnet. Top: selected beam images at different trim-current settings. Bottom: beam centroid position as a function of trim current. Inset A: experimental layout. Inset B: the measured axial magnetic-field profile of the trim magnet used to determine the integrated magnetic field for the momentum estimate.

TABLE III. Comparison of the Nb_3Sn photogun design parameters, vertical-test performance, best conduction-cooled rf performance, and first-beam operating conditions.

Parameter	Design	VTS	CC, Gun only	First beam
E_{acc}	10 MV/m	6 MV/m	4.5 MV/m	3.5 MV/m (inferred)
$E_{cathode}$	20 MV/m	12 MV/m	9 MV/m	7 MV/m (inferred)
$Q_0@E_{acc}$	1.61×10^{10}	2.4×10^9	1.8×10^9	2.4×10^9
Cavity temp. $@E_{acc}$	4 K	4.4 K	5 K	4.8 K
Cold-head temp. $@E_{acc}$	...	...	4.4 K	4.4 K
Estimated cavity rf dissipation $@E_{acc}$	0.9 W	...	1.8 W[a]	1.4 W[a]
Static magnetic field	< 10 mG	< 5 mG	< 10 mG	5 mG
Laser pulse energy	0.23 μJ for 5 fC	...	...	3.7 μJ
Laser spot size	36 μm rms	...	...	10 mm in diameter
Repetition rate	1 MHz	...	...	2 Hz
Bunch charge	5 fC	...	...	Not measured; 80 fC est.
Beam energy	1.6 MeV	...	400 keV sim.	190 keV meas.

[a]Cavity rf power loss without deduction of the rf cable loss due to excessive heat at E_{acc}.

particularly the assumption that the beam passes near the magnetic center, together with uncertainty in the centroid determination. Because the available commissioning data do not support a rigorous uncertainty estimate, the value of 190 keV should be regarded as an approximate estimate. The approximately 400 keV value quoted in Sec. IV represents the simulated maximum beam energy at $E_{acc} \approx 4.5$ MV/m for an appropriate laser injection phase. During the first-beam experiment, stable laser-rf phase locking was not achieved, and the instantaneous cavity field and emission phase were not independently established for each beam event. The available data therefore do not allow the respective contributions of the cavity field and injection phase to the measured beam energy to be separated quantitatively.

Table III summarizes the principal design parameters and the corresponding performance achieved during the Nb_3Sn vertical test, conduction-cooled rf operation, and first-beam experiment.

VI. FUTURE WORK

Future work will focus on recovering cavity performance and advancing toward fully characterized beam operation. Priority will be given to improving Nb_3Sn coating quality and restoring the designed accelerating gradient. In parallel, the laser-rf synchronization system will be upgraded to enable stable phase locking and systematic beam-dynamics measurements. These efforts will support subsequent high-repetition-rate beam studies and move the system closer to practical application in MeV UEM/UED.

VII. CONCLUSION

We have demonstrated the first beam from the world's first conduction-cooled superconducting rf photogun. The developed system combines a 1.3 GHz Nb_3Sn-coated srf photogun, a compact cryogen-free cryomodule, and an integrated beamline, demonstrating that photoemission from a fully conduction-cooled srf photoinjector can be achieved without liquid-helium infrastructure. The successful operation of the photogun validates the feasibility of combining Nb_3Sn cavity technology with cryocooler-based conduction cooling for compact accelerator applications.

During the course of this project, a number of technical challenges associated with Nb_3Sn coating, cryogenic integration, thermal management, magnetic shielding, and beamline assembly were identified and systematically addressed. Despite the reduced cavity performance caused by coating-related issues, stable cryogenic operation was achieved with rf dissipation compatible with the available cryocooler capacity, enabling successful generation of the first photoemitted electron beam. Although MeV beam energy, high-repetition-rate beam operation, and the emittance, energy-spread, and stability requirements for practical UED/UEM remain to be demonstrated, the present work establishes an important technological milestone toward practical cryogen-free srf electron sources. Future efforts will focus on improving the Nb_3Sn coating quality, restoring the cavity to its design accelerating gradient, completing beam synchronization and full beam characterization, and integrating the photogun into a dedicated MeV-UED/UEM beamline. Beyond ultrafast electron imaging, the demonstrated conduction-cooled srf photoinjector architecture provides a scalable platform for compact continuous-wave accelerators in scientific, industrial, and medical applications.

ACKNOWLEDGMENTS

The authors would like to thank the technical staff at Argonne National Laboratory and the Fermilab Technology Directorate for the cavity preparation. Fermilab is managed by Fermi Forward Discovery

Group, LLC under Contract No. 89243024CSC000002 with the U.S. Department of Energy, Office of Science, Office of High Energy Physics. This work was funded by the DOE SBIR program under Contract No. DE-SC0018621.

DATA AVAILABILITY

There are no publicly available research data or software supporting this manuscript. Requests for further information or data should be sent to the authors.

[1] B. J. Siwick, J. R. Dwyer, R. E. Jordan, and R. J. D. Miller, An atomic-level view of melting using femtosecond electron diffraction, Science **302**, 1382 (2003).

[2] R. J. D. Miller, Femtosecond crystallography with ultrabright electrons and x-rays: Capturing chemistry in action, Science **343**, 1108 (2014).

[3] D. Filippetto, P. Musumeci, R. K. Li, B. J. Siwick, M. R. Otto, M. Centurion, and J. P. F. Nunes, Ultrafast electron diffraction: Visualizing dynamic states of matter, Rev. Mod. Phys. **94**, 045004 (2022).

[4] X. Yang, L. Wang, J. Maxson, A. C. Bartnik, M. Kaemingk, W. Wan, L. Cultrera, L. Wu, V. Smaluk, T. Shaftan, S. McSweeney, C. Jing, R. Kostin, and Y. Zhu, Towards construction of a novel nanometer-resolution MeV-STEM for imaging thick frozen biological samples, Photonics **11**, 252 (2024).

[5] P. Musumeci, J. Giner Navarro, J. B. Rosenzweig, L. Cultrera, I. Bazarov, J. Maxson, S. Karkare, and H. Padmore, Advances in bright electron sources, Nucl. Instrum. Methods Phys. Res., Sect. A **907**, 209 (2018).

[6] J. Maxson, D. Cesar, G. Calmasini, A. Ody, P. Musumeci, and D. Alesini, Direct measurement of sub-10 fs relativistic electron beams with ultralow emittance, Phys. Rev. Lett. **118**, 154802 (2017).

[7] J. B. Hastings, F. M. Rudakov, D. H. Dowell, J. F. Schmerge, J. D. Cardoza, J. M. Castro, S. M. Gierman, H. Loos, and P. M. Weber, Ultrafast time-resolved electron diffraction with megavolt electron beams, Appl. Phys. Lett. **89**, 184109 (2006).

[8] P. Musumeci, J. T. Moody, C. M. Scoby, M. S. Gutierrez, H. A. Bender, and N. S. Wilcox, High quality single shot diffraction patterns using ultrashort megaelectron volt electron beams from a radio frequency photoinjector, Rev. Sci. Instrum. **81**, 013306 (2010).

[9] R. K. Li and P. Musumeci, Single-shot MeV transmission electron microscopy with picosecond temporal resolution, Phys. Rev. Appl. **2**, 024003 (2014).

[10] I. Petrushina *et al.*, High-brightness continuous-wave electron beams from superconducting radio-frequency photoemission gun, Phys. Rev. Lett. **124**, 244801 (2020).

[11] J. Teichert, A. Arnold, H. Büttig, M. Justus, T. Kamps, U. Lehnert, P. Lu, P. Michel, P. Murcek, J. Rudolph, R. Schurig, W. Seidel, H. Vennekate, I. Will, and R. Xiang, Free-electron laser operation with a superconducting radio-frequency photoinjector at ELBE, Nucl. Instrum. Methods Phys. Res., Sect. A **743**, 114 (2014).

[12] A. Arnold and J. Teichert, Overview on superconducting photoinjectors, Phys. Rev. ST Accel. Beams **14**, 024801 (2011).

[13] R. Xiang, A. Arnold, and J. W. Lewellen, Superconducting radio frequency photoinjectors for CW-XFEL, Front. Phys. **11**, 1 (2023).

[14] J. R. Harris, K. L. Ferguson, J. W. Lewellen, S. P. Niles, B. Rusnak, R. L. Swent, W. B. Colson, T. I. Smith, C. H. Boulware, T. L. Grimm, P. R. Cunningham, M. S. Curtin, D. C. Miccolis, D. J. Sox, and W. S. Graves, Design and operation of a superconducting quarter-wave electron gun, Phys. Rev. ST Accel. Beams **14**, 053501 (2011).

[15] A. Neumann *et al.*, The bERLinPro SRF photoinjector system–from first RF commissioning to first beam, in *Proceedings of the 9th International Particle Accelerator Conference (IPAC'18)* (JACoW Publishing, Geneva, Switzerland, 2018), p. 1660.

[16] S. Posen, J. Lee, D. N. Seidman, A. Romanenko, B. Tennis, O. S. Melnychuk, and D. A. Sergatskov, Advances in Nb_3Sn superconducting radiofrequency cavities towards first practical accelerator applications, Supercond. Sci. Technol. **34**, 025007 (2021).

[17] R. C. Dhuley, S. Posen, M. I. Geelhoed, O. Prokofiev, and J. C. T. Thangaraj, First demonstration of a cryocooler conduction-cooled superconducting radiofrequency cavity operating at practical CW accelerating gradients, Supercond. Sci. Technol. **33**, 06LT01 (2020).

[18] G. Ciovati, G. Cheng, U. Pudasaini, and R. A. Rimmer, Multi-metallic conduction cooled superconducting radiofrequency cavity with high thermal stability, Supercond. Sci. Technol. **33**, 07LT01 (2020).

[19] R. C. Dhuley, R. Kostin, O. Prokofiev, M. I. Geelhoed, T. H. Nicol, S. Posen, J. C. T. Thangaraj, T. K. Kroc, and R. D. Kephart, Thermal link design for conduction cooling of SRF cavities using cryocoolers, IEEE Trans. Appl. Supercond. **29**, 1 (2019).

[20] Y. Trenikhina, S. Posen, A. Romanenko, M. Sardela, J.-M. Zuo, D. L. Hall, and M. Liepe, Performance-defining properties of Nb_3Sn coating in SRF cavities, Supercond. Sci. Technol. **31**, 015004 (2018).

[21] N. Stilin, A. Holic, M. Liepe, t. O'Connell, J. Sears, V. Shemelin, and J. Turco, Status update on Cornell's SRFcompact conduction cooled cryomodule, in *Proc. 13th International Particle Accelerator Conference (IPAC'22)* (JACoW Publishing, Geneva, Switzerland, 2022), p. 1299.

[22] R. Kostin, C. Jing, S. Posen, T. Khabiboulline, and D. Bice, Nb_3Sn SRF photogun high power test at cryogenic temperatures, IEEE Trans. Appl. Supercond. **33**, 1 (2023).

[23] R. Kostin, C. Jing, E. Knight, Y. Zhao, M. Camarena, S. Posen, G. Eremeev, T. Khabiboulline, D. Bice, and A. Netepenko, First conduction cooled photoinjector status, in *Proc. 15th International Particle Accelerator Conference (IPAC'24)* (JACoW Publishing, Geneva, Switzerland, 2024), p. 2747.

[24] A. Liu, P. Avrakhov, C. Jing, and R. Kostin, Optimization of an SRF gun design for UEM applications, in *Proc. North American Particle Accelerator Conf. (NAPAC'19)* (JACoW Publishing, Geneva, Switzerland, 2019), p. 305.

[25] E. Pirez, P. Musumeci, J. Maxson, and D. Alesini, S-band 1.4 cell photoinjector design for high brightness beam generation, Nucl. Instrum. Methods Phys. Res., Sect. A **865**, 109 (2017).

[26] R. Kostin, C. Jing, P. Avrakhov, Y. Zhao, and A. Liu, Status of conduction cooled SRF photogun for UEM/UED, in *Proc. 12th International Particle Accelerator Conference (IPAC'21)* (JACoW Publishing, Geneva, Switzerland, 2021), p. 1773.

[27] R. Kostin, C. Jing, S. Posen, T. Khabiboulline, and D. Bice, First high-gradient results of UED/UEM SRF gun at cryogenic temperatures, in *Proc. North American Particle Accelerator Conf. (NAPAC'22)* (JACoW Publishing, Geneva, Switzerland, 2022), p. 607.